MOX-Report No. 22/2024

A scalable well-balanced numerical scheme for a depth-integrated lava flow model

Gatti, F.; de Falco, C.; Fois, M.; Formaggia, L.

MOX, Dipartimento di Matematica
Politecnico di Milano, Via Bonardi 9 - 20133 Milano (Italy)

mox-dmat@polimi.it https://mox.polimi.it

A Scalable Well-balanced Numerical Scheme for a Depth-integrated Lava Flow Model

Federico Gatti[a,*], Carlo de Falco[b], Marco Fois[b], Luca Formaggia[b]

[a]Consiglio Nazionale delle Ricerche - Istituto di Matematica Applicata e Tecnologie Informatiche "E. Magenes" (CNR-IMATI), Via Ferrata 1, 27100, Pavia, Italy
federico.gatti@imati.cnr.it
[b] MOX – Modelling and Scientific Computing, Department of Mathematics, Politecnico di Milano, Piazza Leonardo da Vinci 32, 20133 Milano, Italy
{carlo.defalco,marco.fois,luca.formaggia}@polimi.it

Abstract

We propose a scalable well-balanced numerical method to efficiently solve a modified set of shallow water equations targeting the dynamics of lava flows. The governing equations are an extension of a depth-integrated model already available in the literature and proposed to model lava flows. Here, we consider the presence of vents that act as point sources in the mass and energy equations. Starting from a scheme developed in the framework of landslide simulation, we prove its capability to deal with lava flows. We show its excellent performances in terms of parallel scaling efficiency while maintaining good results in terms of accuracy. To verify the reliability of the proposed simulation tool, we first assess the accuracy and efficiency of the scheme on ideal scenarios. In particular, we investigate the well-balancing property, we simulate benchmarks taken from the literature in the framework of lava flow simulations, and provide relevant scaling results for the parallel implementation of the method. Successively, we challenge the scheme on a real configuration taken from the available literature.

Keywords: Taylor-Galerkin scheme, Depth-integrated models, Parallel simulations, Lava flows, Quadtree mesh, Path-conservative method.

1 Introduction

Volcanic eruptions are awe-inspiring natural phenomena, with lava flows representing a prominent aspect of their destructive potential. Understanding and predicting the behavior of lava flows is of paramount importance to enhance our comprehension of volcanic hazards and facilitate decision-making in volcanic risk management. Within this pursuit, mathematical models assume a pivotal role, serving as a tool to simulate and dissect the intricate dynamics of lava flows. Among these models, depth-integrated lava flow models have ascended in importance due to their adeptness in capturing the overarching behavior of lava while maintaining computational efficiency.
The model we consider was first proposed in [1] and later extended in [2, 3]. It can be considered a modification of the classical shallow water system, incorporating the depth-integration of the energy equation from the full Navier-Stokes system. The temperature plays a significant role in lava flow dynamics and cannot be neglected in the modeling phase. The shallow-water model, also known as de Saint-Venant equations, is a set of partial differential equations originally designed to approximate the behavior of fluid flow in situations where the depth of the fluid is much smaller than the horizontal length scales of the system. This approximation has proven particularly useful in the study of various geophysical and environmental phenomena, including but not limited to river hydraulics, flood problems, landslide runout forecasting, see, e.g., [4, 5, 6, 7, 8] and references therein.

In this work, we propose a scalable well-balanced numerical scheme to solve a depth-integrated system of equations modeling lava flow dynamics. The scheme implements a new variant of the classical two-step Taylor-Galerkin (TG2) scheme on adaptive quadtree meshes, named TG2-PC. The acronym PC stands for the Path-Conservative method, widely used in the literature in combination with finite-volume and discontinuous finite-element schemes [9, 10, 11, 12, 13, 14]. The TG2-PC combines the TG2 method on hierarchical quadtree meshes with a novel PC integral on continuous finite element spaces. An appropriate choice of the phase space path is sufficient to guarantee the scheme's exactness with respect to the lake-at-rest solution at the discrete level, i.e., the well-balancing property.
The TG2-PC scheme was introduced in [15], for the solution of a single-phase single-layer depth-integrated landslide model, and later on enriched in [4] for a two-phase two-layer landslide model. In particular, in [15] we decouple the stiff/parabolic from the advection/hyperbolic part through a second-order space-time Strang splitting procedure. While, in [4] the hyperbolic and stiff parts are treated together in an additive Runge-Kutta procedure. In both cases, the scheme has shown excellent results in terms of parallel performances while maintaining good accuracy. Here, we further modify the time integration of the source terms, by considering a different additive time integration scheme. The resulting discretization is proved to be more stable when compared to the one described in [4]. This modification is beneficial from the stability viewpoint of the method as it prevents the time step to go to zero due to the rise of numerical spurious oscillations. Indeed, in the numerical tests we present, especially when dealing with the real case study, the scheme proposed in [4] for the landslide model fails to provide an oscillation free solution. The physical model we consider is a set of nonlinear balance laws with nonconservative contributions. This model is similar to the one considered in [1, 2, 3], but is further enriched with the presence of vents that are modeled as point-wise sources in the depth-integrated model. Vents are openings in the crust of the planet from which lava erupts.

The paper is organized as follows: In section 2, we present the physical model considered. In section 3, we describe the numerical model adopted to discretize the mathematical model. In section 4, the proposed discretization scheme is applied to several tests, in which the accuracy of the numerical schemes is studied. The concluding remarks are presented in section 5.

2 Physical model

According to [1, 2, 3] lava flow can be modeled with a set of equations obtained from the depth-integration of the Navier-Stokes equations considering a hydrostatic pressure distribution along the vertical axis. This idea stems from the hypothesis that the vertical length-scale of the flowing material is much smaller than the horizontal one.

We consider a Cartesian domain $\Omega = (0, L_x) \times (0, L_y) \subset \mathbb{R}^2$ and a domain $\Omega_w \subset \Omega$, which moves in space and time and is defined as the space where the lava height is greater than zero, i.e., $h > 0$. According to [16], in $\Omega_w \times (0, t_{\text{fin}}]$, t_{fin} being the final time, we define the following depth-integrated model, which is basically the shallow water system for the mass and momentum, plus another equation modeling the evolution of the temperature during the lava movement

$$\begin{cases} \partial_t h + \partial_x(hu_x) + \partial_y(hu_y) = Q\delta(\mathbf{x} - \mathbf{x}_v), \\ \partial_t(hu_x) + \partial_x\left(hu_x^2 + \frac{1}{2}gh^2\right) + \partial_y\left(hu_x u_y\right) + gh\partial_x Z = -\gamma u_x, \\ \partial_t(hu_y) + \partial_x\left(hu_y u_x\right) + \partial_y\left(hu_y^2 + \frac{1}{2}gh^2\right) + gh\partial_y Z = -\gamma u_y, \\ \partial_t(hT) + \partial_x\left(hTu_x\right) + \partial_y\left(hTu_y\right) = QT_e\delta(\mathbf{x} - \mathbf{x}_v). \end{cases} \tag{1}$$

Apart from the material height h that we have already defined above, the unknowns are represented by the mass fluxes along the x- and y-direction hu_x, hu_y respectively and by hT, which is the product between the depth-integrated temperature and the material height, i.e.,

$$hT = \int_Z^{Z+h} \mathcal{T}(x, y, z)\, dz, \tag{2}$$

where $\mathcal{T} = \mathcal{T}(x, y, z)$ is the vertically varying temperature, solution of the Navier-Stokes system. As underlined in [2], the transport terms of the momentum and energy equations can be modified by considering multiplicative coefficients known as Boussinesq or shape factors. Nevertheless, the presence of these coefficients slightly modify the eigenvalues of the Jacobian matrix associated to the transport operator without compromising its analytical computation. To make an example, under the hypothesis of parabolic profile in the vertical direction, the momentum shape factors reduce to $\frac{6}{5}$. These shape factors correspond to 1 only in case a constant vertical profile is assumed. Here, for simplicity, we set these coefficients to 1 since they do not alter the numerical scheme we present.

Concerning the reaction term, we have a quantity $Q\delta(\mathbf{x}-\mathbf{x}_v)$ in the mass conservation equation, where δ is the Dirac's delta and $\mathbf{x}_v$ is the vent spatial location. The quantity Q represents the lava discharge into the domain and could be a time varying function. The effect of the vent reflects also in the energy equation where appears $QT_e\delta(\mathbf{x} - \mathbf{x}_v)$, where T_e is the vent effusion temperature. In the friction term appearing in the momentum equation, we define the dimensionless coefficient $\gamma = k_*/[1 + k_* h/(3\nu_r)]$, according to [17, 18], where ν_r is a reference kinematic viscosity, i.e., it is evaluated at a reference temperature T_r, and k_* is the Navier friction coefficient. In the present work, by considering the following dynamic viscosity

$$\mu = \mu_r e^{-b(T-T_r)}, \tag{3}$$

and in the limit case $k_* h/\nu_r \gg 1$, implying that $\gamma = 3\nu/h$, we obtain the approximation

$$\gamma = \frac{3\nu_r}{h} e^{-b(T-T_r)}. \tag{4}$$

The quantity ν_r is the reference kinematic viscosity, and is linked to the μ_r through the lava density ρ, i.e., $\mu_r = \nu_r \rho$. According to [1], a convenient choice for the reference temperature coincides with the vent effusion temperature.

Possibly, other reaction terms could be considered in the energy equation. We mention the conductive, radiative, convective, and viscous heating coefficient. These terms represent the energy dissipation of the lava during its motion due to heat transfer and internal stresses, and are important to conduct a real case study analysis. Indeed, they improve the dissipation rate of the temperature of the flowing material, and enrich the model with calibration parameters that can be useful when performing back analysis. In this study, we simply neglect them and focus on the presence of the friction coefficient on the momentum equation that depends on the temperature, and plays a significant role in the coupling between the momentum and energy equations. Anyway, the heat transfer contributions can be easily inserted in the numerical method we present in this work without requiring any modification of the conceptual scheme.

Finally, we notice that this depth-integrated system of equations (1) admits the following steady state solution

$$h + Z = \text{constant}, \quad \mathbf{u} = \mathbf{0}, \quad T = \text{constant}, \tag{5}$$

which is normally named lake-at-rest condition. One of the goals of the numerical method we propose in this work is to be exact with respect to this lake-at-rest condition. In the literature, numerical schemes that are built to be exact to this condition are named well-balanced schemes.

3 Numerical scheme

We note that system of equations (1) can be written as a hyperbolic system of equations where non-conservative terms and algebraic sources are present, i.e.,

$$\partial_t \mathbf{q} + \nabla \cdot \mathbf{F} + \mathbf{B}\nabla Z = \mathbf{S}, \tag{6}$$

where the vector of conserved quantities reads,

$$\mathbf{q} = \begin{bmatrix} h \\ hu_x \\ hu_y \\ hT \\ Z \end{bmatrix}. \tag{7}$$

The term $\mathbf{F} = \mathbf{F}(\mathbf{q})$ corresponds to the tensor of transport fluxes,

$$\mathbf{F}(\mathbf{q}) = \begin{bmatrix} hu_x & hu_y \\ hu_x^2 + \frac{1}{2}gh^2 & hu_x u_y \\ hu_y u_x & hu_y^2 + \frac{1}{2}gh^2 \\ hTu_x & hTu_y \\ 0 & 0 \end{bmatrix}, \tag{8}$$

the tensor $\mathbf{B} = \mathbf{B}(\mathbf{q})$ representing the non-conservative matrix reads

$$\mathbf{B}(\mathbf{q}) = \begin{bmatrix} 0 & 0 \\ gh & 0 \\ 0 & gh \\ 0 & 0 \\ 0 & 0 \end{bmatrix}, \tag{9}$$

while the source term $\mathbf{S} = \mathbf{S}(\mathbf{q})$ is

$$\mathbf{S}(\mathbf{q}) = \begin{bmatrix} Q\delta(\mathbf{x} - \mathbf{x}_v) \\ -\gamma u_x \\ -\gamma u_y \\ QT_e\delta(\mathbf{x} - \mathbf{x}_v) \\ 0 \end{bmatrix}. \tag{10}$$

According to the works [6, 15, 7], we set a numerical threshold $h_{\min}$ on the material height so to provide a discretization of the wet region Ω_w so that, in regions below $h_{\min}$, the model equations modify as

$$\begin{aligned} \partial_t h &= 0, \\ hu_x &= 0, \\ hu_y &= 0, \\ hT &= 0. \end{aligned} \tag{11}$$

A great advantage of this procedure is that we can extend to the whole computational domain Ω the solution of the system of equations (1), and outflow boundary conditions are applied naturally at the boundary of the discrete wet region Ω_w.

The numerical method we adopt is a modification of the classical two-step Taylor-Galerkin (TG2) method, namely the second-order Taylor-Galerkin Path-Conservative (TG2-PC) method on adaptive quadtree meshes. This method has been developed by some of the authors and has already been successfully applied to solve depth-integrated problems describing the landslide runout phase, see [6, 15, 4]. The TG2-PC scheme exploits the excellent scaling performances of the TG2 scheme, while employing the Path-Conservative (PC) strategy to the computation of non-conservative products through a novel implementation on continuous finite-element spaces.

According to what done for the solution of the two-phase consolidation landslide model [4], the presence of the reaction term implies a potential source of stiffness. So, the application of the TG2-PC strategy to the complete system would require the adoption of a time step considerably smaller than the one needed to discretize the transport fluxes, eventually leading to a greater diffusion error when resolving advection features. Nevertheless, we note that in most of the real cases discretizing stiff sources often leads to time steps numerically close to zero. To overcome this stiffness, we combine the Taylor time series expansion of the TG2-PC method with a second-order L-stable time integration for the source term. This combination is performed in an IMplicit EXplicit (IMEX) Additive Runge-Kutta (ARK) method, by resorting on the Additive RK.2.L.1 scheme developed in [19]. This method enables the efficient treatment of fast, reaction term, and slow, hyperbolic operator, dynamics separately. The complete Butcher's tableau reads,

$$\begin{array}{c|c|c} \mathbf{c} & \tilde{\mathbf{A}} & \mathbf{A} \\ \hline & \tilde{\mathbf{b}}^T & \mathbf{b}^T \end{array} = \begin{array}{c|ccc|ccc} 0 & 0 & 0 & 0 & 0 & 0 & 0 \\ \frac{1}{2} & \frac{1}{2}(-1+\sqrt{2}) & 1-\frac{\sqrt{2}}{2} & 0 & \frac{1}{2} & 0 & 0 \\ 1 & 1-\frac{\sqrt{2}}{2} & \sqrt{2}-1 & 1-\frac{\sqrt{2}}{2} & 0 & 1 & 0 \\ \hline & 1-\frac{\sqrt{2}}{2} & \sqrt{2}-1 & 1-\frac{\sqrt{2}}{2} & 0 & 1 & 0 \end{array}, \tag{12}$$

where the left arrays $(\tilde{\mathbf{A}}, \tilde{\mathbf{b}})$ interests the discretization of the stiff source term, while the right one $(\mathbf{A}, \mathbf{b})$ is the Taylor-type discretization and is used to discretize the hyperbolic transport term. The effectiveness of IMEX schemes have been demonstrated in several computational physics contexts, from magnetized plasma flows [20] to atmospheric applications [21, 22] and fluid dynamics of incompressible flows [23].

Let us consider a time step Δt, the temporal approximations of the conserved variable $\mathbf{q}^n$, $\mathbf{q}^{n+\frac{1}{2}}$, $\mathbf{q}^{n+1}$ at times t^n, $t^{n+\frac{1}{2}}$, t^{n+1}, respectively. Then, the quantities with the superscript n, $n+\frac{1}{2}$, $n+1$ indicate the evaluation of the quantities themselves in the discrete conserved variable in time $\mathbf{q}^n$, $\mathbf{q}^{n+\frac{1}{2}}$, $\mathbf{q}^{n+1}$, respectively. To obtain the fully discrete system, consider a quadtree mesh partition and identify with M the number of quadrilateral mesh elements, while with N the number of active nodes. The set of active nodes refers to the total number of nodes minus the set of

hanging nodes. We seek solutions at integer times, t^n, t^{n+1}, in the continuous space $\tilde{\mathbb{Q}}_1$ and for half-time solutions in the piecewise discontinuous space $\mathbb{Q}_0$ as defined in [6]. In this way, by integrating by parts the conservative transport fluxes appearing in the second step of the method, and by indicating with $(\cdot,\cdot)$ the $L^2(\Omega)$-scalar product and by $\mathbf{n}$ the unit outward normal vector to the boundary $\partial\Omega$ of Ω, we obtain the following fully discrete weak-form

$$
\begin{aligned}
(\mathbf{q}^{n+\frac{1}{2}},\phi_j^{(0)}) &= (\mathbf{q}^n,\phi_j^{(0)}) - \frac{\Delta t}{2}\,(\nabla\cdot\mathbf{F}^n,\phi_j^{(0)}) - \frac{\Delta t}{2}\,(\mathbf{B}^n\nabla\mathbf{q}^n,\phi_j^{(0)}) + \frac{\Delta t}{2}\left(-1+\sqrt{2}\right)\,(\mathbf{S}^n,\phi_j^{(0)}) \\
&\quad + \Delta t\left(1-\frac{\sqrt{2}}{2}\right)\,(\mathbf{S}^{n+\frac{1}{2}},\phi_j^{(0)}), \\
(\mathbf{q}^{n+1},\tilde{\phi}_i^{(1)}) &= (\mathbf{q}^n,\tilde{\phi}_i^{(1)}) + \Delta t\,(\mathbf{F}^{*,n+\frac{1}{2}},\nabla\tilde{\phi}_i^{(1)}) - \Delta t\,(\mathbf{B}^{n+\frac{1}{2}}\nabla\mathbf{q}^{n+\frac{1}{2}},\tilde{\phi}_i^{(1)}) - \Delta t\int_{\partial\Omega}\mathbf{F}^{*,n+\frac{1}{2}}\,\mathbf{n}\,\tilde{\phi}_i^{(1)}\,d\Sigma \\
&\quad + \Delta t\left(1-\frac{\sqrt{2}}{2}\right)\,(\mathbf{S}^n+\mathbf{S}^{n+1},\tilde{\phi}_i^{(1)}) + \Delta t\left(\sqrt{2}-1\right)\,(\mathbf{S}^{n+\frac{1}{2}},\tilde{\phi}_i^{(1)}),
\end{aligned}
\tag{13}
$$

where the set $\{\tilde{\phi}_i^{(1)}\}_{i=1}^N$ refers to the set of basis functions of the space $\tilde{\mathbb{Q}}_1$, while $\{\phi_j^{(0)}\}_{j=1}^M$ refers to the set of basis functions of the space $\mathbb{Q}_0$. In A, the reader can find details of the asymptotic stability of the scheme (13) in case of severe stiffness of the source terms, for the linear scalar conservation equation with linear sources. We study the asymptotic behaviour of the amplification factor of the present scheme in comparison to the scheme presented in n [4]. We note that, in the formulation above (13), we have put in the second step of the scheme a flux $\mathbf{F}^{*,n+\frac{1}{2}}$ which refers to a discrete flux function of $\mathbf{F}^{n+\frac{1}{2}}$ but modified to ensure an oscillation-free solution according to the flux correction limiting procedure (FCT) procedure. Thus, the discrete numerical flux reads

$$
\mathbf{F}^{*,n+\frac{1}{2}} = (\mathbf{F}^{n+\frac{1}{2}} - \delta\mathbf{F}^n) + \phi\delta\mathbf{F}^n, \tag{14}
$$

with $\delta\mathbf{F}^n$ the anti-diffusive flux to be defined later, giving the diffusive contribution $-\delta\mathbf{F}^n$ to the high order discrete flux $\mathbf{F}^{n+\frac{1}{2}}$ in equation (14), and ϕ the piecewise constant FCT coefficient defined according to the Zalesak's procedure [24, 25, 26], specifically by following the quadtree version in [6]. By applying the mass lumping procedure in the second step of the scheme (13), we can formally proof that, in one space dimension and in the case $\phi = 0$, this discretization coincides with the Lax-Wendroff scheme, thus it is subject to the standard CFL condition on the transport term. In this work, we choose the time step accordingly. The anti-diffusive flux is computed according to the Rusanov numerical flux but suitably modified to take into account the the scheme to be exact to the lake-at-rest condition (5). Inspired by the work [27] and as already done to discretize the two-phase consolidation landslide model [4], with reference to a single mesh element, say j, having extension Δx_j and Δy_j along the x- and y-direction, respectively, we propose the following well-balanced modification of the Rusanov numerical flux,

$$
\delta\mathbf{F}_j^n = \min_{\left(\frac{\Delta x_j}{\Delta t},\frac{\Delta y_j}{\Delta t}\right)}\frac{1}{2\Delta t}(\nabla\mathbf{v}^n,\phi_j^{(0)}), \tag{15}
$$

where vector $\mathbf{v}^n$ is the time-discrete counterpart of the vector $\mathbf{v}$, which is linked to the vector $\mathbf{q}$ of the conserved variables through the relation $\mathbf{v} = \mathbf{U}\mathbf{q}$, with $\mathbf{U}$ the transformation matrix given by

$$
\mathbf{U} = \begin{bmatrix} 1 & 0 & 0 & 0 & 1-u \\ 0 & 1 & 0 & 0 & 0 \\ 0 & 0 & 1 & 0 & 0 \\ 0 & 0 & 0 & 1 & 0 \\ 0 & 0 & 0 & 0 & 0 \end{bmatrix}. \tag{16}
$$

Here, $u = u(|\nabla\eta| - h_{\min})$ denotes the Heaviside step function, $\eta = H + Z$ and η^n is the time discrete counterpart. Moreover, in the computation of the anti-diffusive Rusanov numerical flux (15), quantities $\Delta x_j/\Delta t, \Delta y_j/\Delta t$ are upper bounded, thanks to the CFL condition, by the maximum simple wave speed in both the directions.

A final step to ensure well-balancing, is the discretization of non-conservative fluxes. We note that the main issue is the computation of these products at the second step of the TG2-PC method $(13)_2$ since the gradient is not defined on the space $\mathbb{Q}_0$. To overcome such a problem, we adopt the same approach used in [15] to model a single-phase depth-integrated landslide model. To this aim, we consider the linear path

$$
\mathbf{\Psi} = \mathbf{\Psi}(\mathbf{q}_-^{n+\frac{1}{2}},\mathbf{q}_+^{n+\frac{1}{2}},s) = \mathbf{q}_-^{n+\frac{1}{2}} + s(\mathbf{q}_+^{n+\frac{1}{2}} - \mathbf{q}_-^{n+\frac{1}{2}}), \tag{17}
$$

parametrized by the real parameter $s \in [0,1]$, which connects two adjacent states, $\mathbf{q}_-^{n+\frac{1}{2}}$, $\mathbf{q}_+^{n+\frac{1}{2}}$, associated with the mesh elements sharing the generic edge e, with barycenter located at $\mathbf{x}_-$ and $\mathbf{x}_+$, respectively. Then, the PC finite element formulation for the integral of the non-conservative products in $(13)_2$ reads

$$
(\mathbf{B}^{n+\frac{1}{2}}\nabla\mathbf{q}^{n+\frac{1}{2}},\tilde{\phi}_i^{(1)}) = \sum_{e\in\mathcal{E}_i}\left(\mathbf{q}_+^{n+\frac{1}{2}} - \mathbf{q}_-^{n+\frac{1}{2}}\right)\int_e\tilde{\phi}_i^{(1)}dl\int_0^1\mathbf{B}(\mathbf{\Psi}(\mathbf{q}_-^{n+\frac{1}{2}},\mathbf{q}_+^{n+\frac{1}{2}},s))\mathbf{n}_e\,ds, \tag{18}
$$

where $\mathcal{E}_i$ denotes the set of all the elements sharing the node i, $\mathbf{n}_e$ is the unit outward normal vector to the edge e, such that $\mathbf{n}_e\cdot(\mathbf{x}_+ - \mathbf{x}_-) > 0$. We compute PC integral through the trapezoidal rule.

Furthermore, we point out that we modify the implicit treatment of the source term in the first and second steps of the method to decouple the momentum from the energy equation. We propose a semi-implicit treatment. In this way, we first compute the mass equation, then integrate the momentum balance where the right-hand side does depend only on the unknown updated mass flux. In particular, the momentum balance equation becomes completely linear since the friction coefficient γ is a linear function of the mass flux. Finally, we solve the energy equation. We note that, a potential presence of non-linear reaction terms in the energy equation can be easily handled by the proposed scheme. Indeed, their presence would have result in a non-linear equation to be solved for the unknown temperature. This procedure is carried out in both steps of the scheme (13), so to compute both $\mathbf{q}^{n+\frac{1}{2}}$ and $\mathbf{q}^{n+1}$.

4 Numerical simulations

In this section, we focus on both benchmark and realistic configurations in order to verify the capability of the proposed numerical scheme to deal with academic problems as well as with real scenarios.
In all simulations, we set $h_{\min} = 10^{-5}$m and keep the CFL number equal to 0.9. Furthermore, in the tests where we resort to a mesh adaptation procedure, if not otherwise stated, we set a tolerance on the solution accuracy equal to 10^{-5}m.

While integrating the source terms appearing in the discrete weak-form, see equation (13), we approximate the Dirac's delta by means of the Gaussian function,

$$f_v(r) = \frac{1}{2\pi\sigma} \exp\left(-\frac{r^2}{2\sigma}\right), \quad \text{with } r^2 = (x - x_v)^2 + (y - y_v)^2, \tag{19}$$

where σ is a parameter having the dimension of area and that can be set by the user. Further, the integrals appearing in the discrete weak-form related to the vent point sources, both in the first and second step of the method, can be integrated explicitly by resorting on the error function. We employ the error function implemented in the C++ standard library.

4.1 Reliability tests

With a first set of simulations we aim to numerically investigate some properties of the proposed discretization scheme when applied to the lava flow model. In more detail, we test the well-balancing property on reference configurations taken from the literature, we carry out a classical viscous dam-break test over flat bottom together with a parallel efficiency test on it. The primary aim is to show the excellent scaling results of the proposed scheme, while maintaining good results in terms of accuracy. Then, we consider a more realistic test where the lava is poured into the domain from a vent and encounters an obstacle during its motion.
All the test are performed in double precision. The strong scaling analysis is executed on the supercomputer CINECA GALILEO100, where we perform the compilation and linking steps with gcc-10 and OpenMPI 4.1.1.

4.1.1 Well-balancing tests

To numerically verify the well-balancing property of the proposed scheme, we analyze two examples with a smooth and a discontinuous topography, respectively. The tests are taken from [28] and have already been reproduced by the authors to investigate the well-balancing property in the framework of landslide runout simulation [15, 4].

	$L^1(\Omega)$-norm of the error				$L^\infty(\Omega)$ -norm of the error			
	h	hu_x	hu_y	hT	h	hu_x	hu_y	hT
Z_1	1.67e-13	4.87e-12	1.48e-12	8.88e-15	1.77e-13	1.21e-13	1.77e-13	1.21e-13
Z_2	1.54e-15	2.78e-13	1.52e-13	3.55e-15	4.48e-14	5.76e-14	4.48e-14	5.76e-14

Table 1: Well-balancing tests. $L^1(\Omega)$- and $L^\infty(\Omega)$-norm of the error for the stationary solution in the presence of a smooth and of a discontinuous bed topography.

We consider a final time $t_{\text{fin}} = 0.5$s and a square domain with horizontal and vertical dimension $L_x = L_y = 10$m; the smooth topography is described by

$$Z(\mathbf{x}) = Z_1(\mathbf{x}) = 5e^{-\frac{2}{5}(x-5)^2}, \tag{20}$$

while the discontinuous one is characterized by the function

$$Z(\mathbf{x}) = Z_2(\mathbf{x}) = \begin{cases} 4 & \text{if } 4 \leq x \leq 8, \\ 0 & \text{otherwise.} \end{cases} \tag{21}$$

Concerning the initial data, we assume lava at rest condition, with a total free surface height equal to 10m, while the quantity hT is initialized to 1000m·K in the whole domain. The domain is discretized with a structured mesh consisting of 2^{14} elements. We do not consider any source term in the present test.
Table 1 provides the $L^1(\Omega)$-norm and $L^\infty(\Omega)$-norm of the error associated with the lava height, and the mean horizontal velocities and temperature, for both the considered topographies. All the errors are close to the roundoff unit, independently of the selected bed profile. This confirms the well-balancing property of the proposed discretization scheme for the lava flow model equations.

4.1.2 Viscous dam-break problem over a flat bottom

We consider a viscous fluid with a Newtonian rheology flowing over a horizontal domain of length $L_x = L_y = 75$m. We set isothermal conditions, meaning that the energy equation does not play any role and assume $T = T_r$, with T_r set equal to zero. The material is initially at rest and with the following initial material height,

$$h = \begin{cases} H & \text{if } x < L, \\ 0 & \text{otherwise.} \end{cases} \tag{22}$$

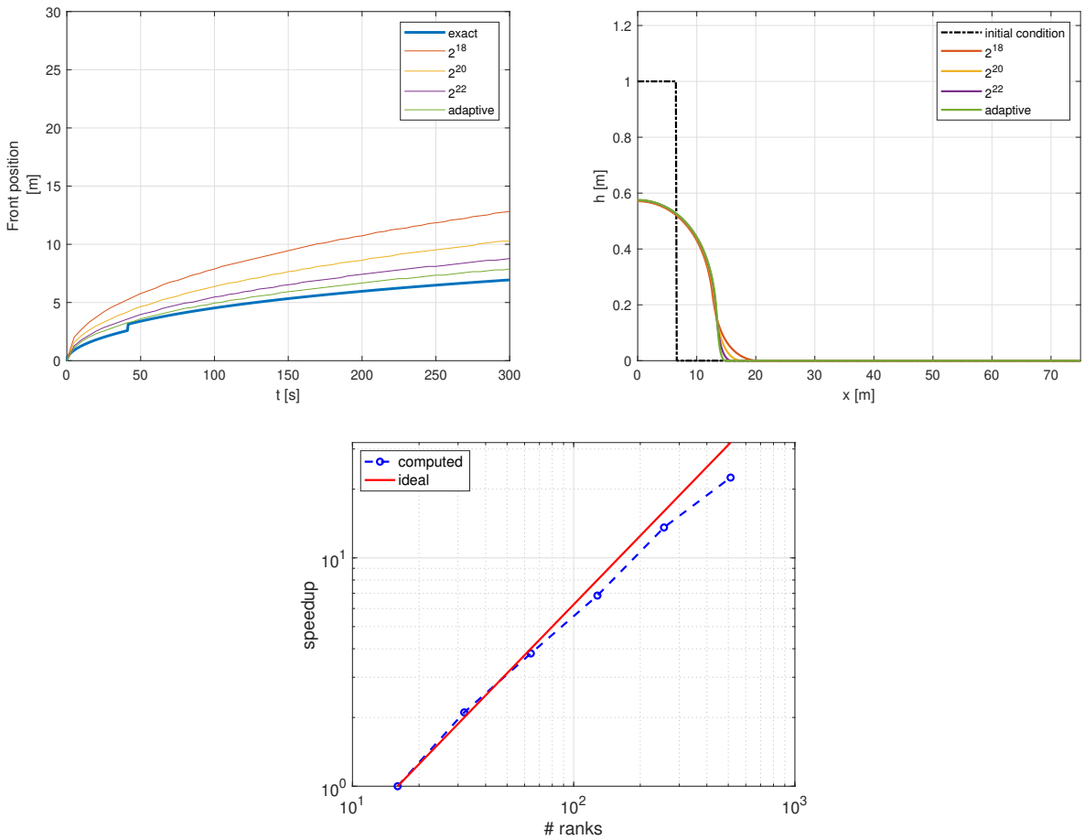

Figure 1: Viscous dam-break problem over a flat bottom. Top-left panel shows the front position over time. Top-right panel reports the final time one-dimensional solution of the material height extracted along the line $y = 37.5$m. Bottom panel shows a strong scaling analysis.

When the flow is slow enough to neglect inertia, it is possible to find analytic solutions. According to [29], in this situation the front evolution is described by the following power law with exponent 0.5, for short times, and 0.2 for long times, i.e.,

$$\frac{x_f(t)}{L} \approx \begin{cases} 0.284 \left(\dfrac{t}{t_c}\right)^{0.5} & \text{if} \quad t < 2.5\, t_c, \\ 1.133 \left(\dfrac{t}{t_c} + 1.221\right)^{0.2} - 1 & \text{otherwise}, \end{cases} \tag{23}$$

where the characteristic time reads $t_c = \left(\dfrac{L}{H}\right)^2 \dfrac{\nu_r}{gH}$. In the following, we set $H = 1$m, $L = 6.6$m, $\nu_r = 3.7\text{m}^2/\text{s}$, and a final time $t_{\text{fin}} = 300$s.

This examination was previously assessed in [2] using a one-dimensional simulation. In our study, we employ four distinct grids: three structured ones, specifically a quadtree mesh with a single level of refinement, and an adaptive grid. The adaptive mesh procedure is performed each 0.1s. The structured grids contain 2^{18}, 2^{20}, 2^{22} elements, while the finest cell resolution equal to $0.018\text{m}\times 0.018\text{m}$. figure 1, at the top, reports the results of our analysis where we extract a one-dimensional solution along the line $y = 37.5$m. In particular, left panel shows the convergence to the analytical solution of the front position, see equation (23). The front position of the numerical solutions is determined by a threshold value on h equal to 10^{-3}m according to what done in [2].

To test the parallel efficiency of the proposed numerical scheme, we perform a strong scaling analysis on the present case study. We focus on the static mesh with 2^{22} elements and set a final time $t_{\text{fin}} = 10$s. We carry out a strong scaling analysis, from 16 to 512 MPI ranks. figure 1, at the bottom, shows the speedup trend as a function of the number of ranks in a `log10-log10` scale. A parallel efficiency of roughly 70% is reached, with an increment close to the ideal one.

4.1.3 Pouring of lava from a vent over an axially symmetric bottom with discontinuity

We consider a more realistic situation in which we have non-isothermal conditions and a vent pouring lava in the domain. The initial condition is no lava in the domain. So, lava is poured in the domain just from the vent.
The domain Ω has extensions along the x- and the y-direction equal to $L = L_x = L_y = 200$m. Lava enters the domain from a vent located at $\mathbf{x}_v = (L/2, L/2)$ with a discharge $Q = 200\text{m}^3/\text{s}$, a temperature $T_e = T_r = 1000$K, a reference viscosity $\nu_r = 2\text{m}^2/\text{s}$, and a coefficient $b = 10^{-3}\text{K}^{-1}$. The parameter σ in (19) has been set equal to 10^{-1}m^2. We perform the simulation with adaptive mesh strategy by imposing a minimum spatial resolution equal to 0.19m, and a tolerance on the accuracy of the space adaptation procedure equal to 10^{-2}m. The mesh adaptation procedure has been carried out at each time step. The topography profile has the form

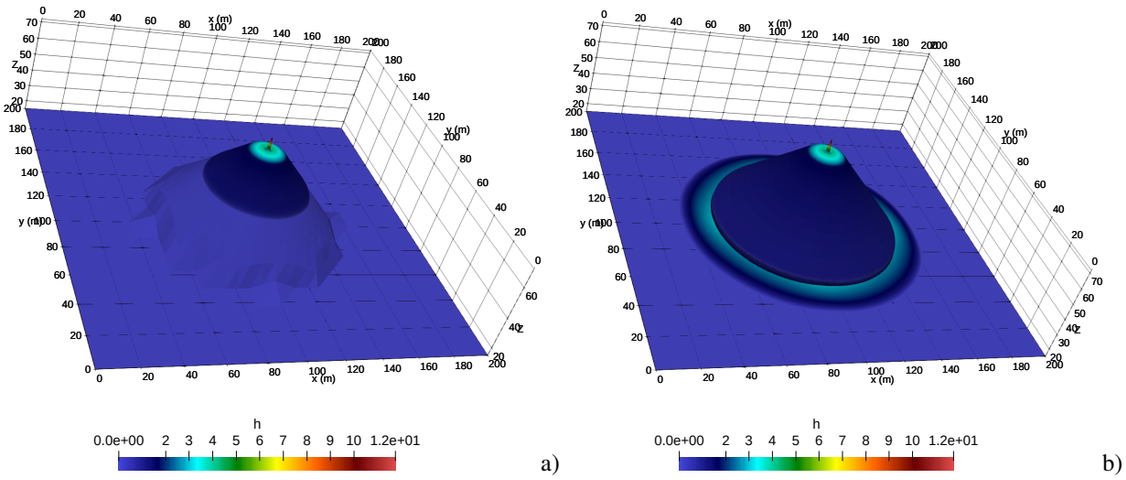

Figure 2: Pouring of lava from a vent over an axially symmetric bottom with discontinuity. Material height superimposed to the topography for two different time instants, $t = 20$s (panel a)) and $t = 100$s (panel b)).

$$Z(r) = \begin{cases} 60 & \text{if } r \leq 10, \\ -r + 70 & \text{if } 10 < r \leq 50, \\ 15 & \text{otherwise,} \end{cases} \qquad \text{with } r = \sqrt{(x - L/2)^2 + (y - L/2)^2}. \tag{24}$$

Figure 2 shows the material height superimposed to the topography profile for two simulation times $t = 20$s (panel a)) and $t = 100$s (panel b)). We particularly note how the topography is properly refined as the flow propagates.
Figure 3 panel a) shows the one-dimensional solution extracted along the line $y = L/2$ of the material height h, of the mass flux U_x, and of the energy flux hT. Note the presence of the vent located at $x_v = 100$m that pours lava in the domain. This reflects on the behaviour of the mass flux that propagates from the left and from the right in the proximity of the vent. Initially, this propagation is due to inertial forces, thanks to the lava inlet from the poring location. In panel b) we show the quadtree mesh at time $t = 100$s. We note how the proposed numerical scheme seems to be able to preserve the axial symmetry of the problem. Further, the horizontal line represents the line where we extract the one-dimensional solution shown in figure 3 panel a).

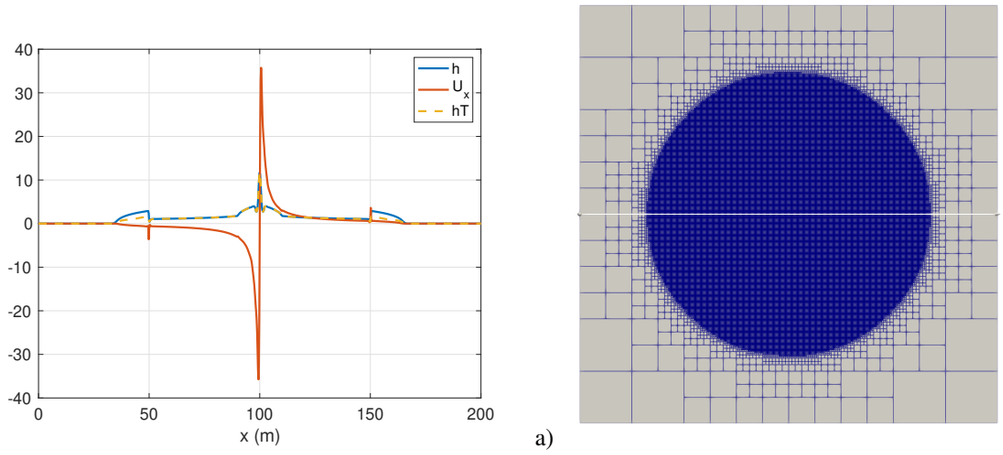

Figure 3: Pouring of lava from a vent over an axially symmetric bottom with discontinuity. Panel a): solution of the material height h (in m), of the mass flux U_x (in m^2/s), and of the energy flux hT (in km K) along the line $y = L/2$. Panel b) plot of the quadtree mesh at the final time $t = 100$s; the horizontal ine is the line where we extract the one-dimensional solution shown in panel a).

4.2 Etna eruption

We focus on reproducing a real eruption interesting the Mount Etna, located in Sicily (Southern Italy).
The topography considered here was taken from [30] and comes from a Digital Elevation Model (DEM). It has a spatial resolution $\Delta = 2$m both in x- and y-directions, and was acquired on December 24, 2015. The event we want to reproduce has been named in the aforementioned article as *flow b*, and happened on 18-19 May, 2016. We refer to figure 4 for a plot of the topography isolines together with the location of the vent indicated with a gray sphere. Further, the black points represent the boundary of the domain touched by the lava during the event. These points are extracted using a digitizer software [31] from the results reported in [30].
Up to our knowledge this is the first time one attempts to reproduce such event with a numerical simulation. So, regarding the rheological parameters, we choose: $\nu_r = 3$m^2/s, $b = 10^{-3}$K^{-1}. Then, the lava is assumed to enter the domain with a discharge $Q = 50$m^3/s and a temperature $T_e = 1000$K. The parameter σ has been set equal to 2m. We run the simulation up to 5000s, we set a tolerance $h_{\min} = 10^{-2}$m and consider a tolerance on the space adaptation procedure equal to 10^{-2}m.

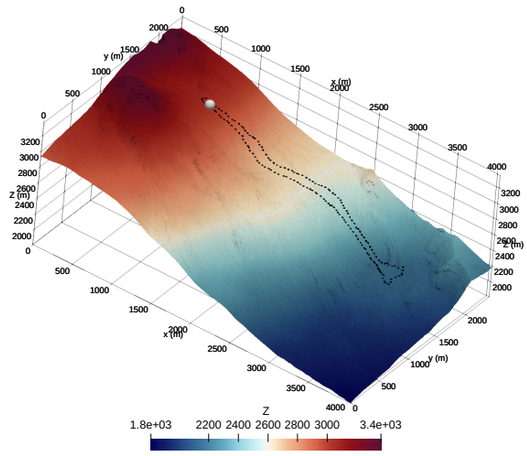

Figure 4: Etna eruption. DEM isolines with the vent location (gray sphere). The black points represent the boundary of the domain touched by the lava during the event.

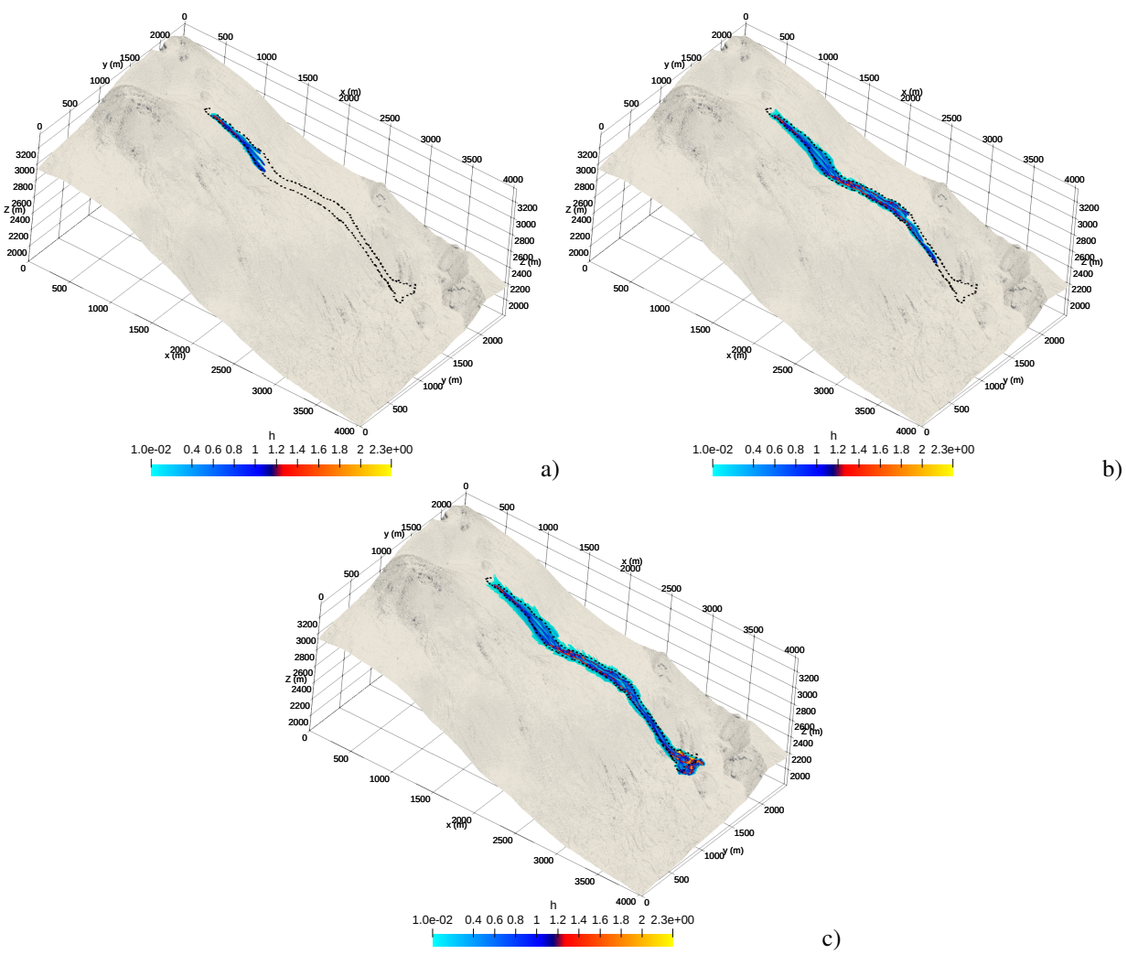

Figure 5: Etna eruption. Isolines of the material height overlapped to the DEM isolines at time $t = 750$s, 3000s, 5000s (from a) to c) panels). The black points represent the boundary of the domain touched by the lava during the event.

Figure 5 shows the isolines of the material height from a minimum value of 1cm superimposed to the DEM isolines at three different times ($t = 750$s, 3000s, 5000s). We observe that the simulated lava flow path remains delimited by the set of black points taken from [30]. In particular, at the end of the simulation the lava covers the whole region delimited by the set of black points. Another similarity with what has been observed in [30] is that the lava accumulates mostly close to the vent location, at the middle of the flow path, and at the end of the runout path, see figure 5 panel c). Of course changes in the rheological and flow discharge parameters (ν_r, b, Q, T_e), change considerably the time the lava takes to reach the full runout distance experienced in [30], and possibly the runout distance itself. Certainly, researchers are expected to conduct uncertainty quantification analysis on these parameters in absence of real observations. In any case, results concerning the lava flow path that remains delimited by the set of black points, and the lava accumulation, which mostly depends on the topography discretization, seem promising.

Finally, we point out that the adoption of the present IMEX-ARK scheme combined with the discrete spaces $\mathbb{Q}_0$, $\tilde{\mathbb{Q}}_1$ was crucial to carry on the simulation. Indeed, we have experienced the rise of numerical spurious oscillations when performing the simulation with the scheme additive scheme considered in [4]. Oscillations that result in the time step to numerically going to zero.

5 Conclusions

We studied a modified set of shallow water equations targeting lava flows simulation. These model equations were first proposed in [1] and later on considered in [2, 3]. In this work, we further enrich the modelling by considering the presence of vents as point sources in the mathematical model. This enables the inlet of masses to the domain directly from these points rather than by imposing an initial condition. We have presented a second-order scalable well-balanced space-time discretization scheme, which solves the non-linearities in the source term through an IMEX-ARK technique for the temporal discretization. The scheme employed is a modification of the one presented in [15, 4], with the aim to provide a greater stability when dealing with severe stiffness of the sources. The proposed fully discrete scheme results to be more stable in case of severe stiffness when compared with the one proposed in [4]. Indeed, we point out that the adoption of this new time integration scheme was crucial to prevent the rise of spurious oscillations in the discretization of the momentum equations, particularly when simulating the real case study presented in section 4.2. An asymptotic stability analysis of the proposed scheme is provided in A, with a comparison with the original discretization presented in [4].

We have tested the proposed numerical method on idealized as well as on realistic DEM scenarios. In particular, we have numerically verified the well-balancing property, the parallel efficiency and the capability to deal with discontinuous topographies. In particular, we have shown the ability of the scheme to deal with real problems as well as the ability to track the progression of lava by using adaptable quadtree meshes.

Possible future developments include exploiting the parallel efficiency of the new method to apply an uncertainty quantification analysis to real case studies, for instance, by resorting to a polynomial chaos expansion [32].
We also note the possibility to construct a fully L-stable discretization of the source terms when combined with the TG2-PC scheme.

Acknowledgements

All authors are members of the Gruppo Nazionale Calcolo Scientifico-Istituto Nazionale di Alta Matematica (GNCS-INdAM).

This research was supported by the Accordo Attuativo ASI-POLIMI "Attività di Ricerca e Innovazione" n. 2018-5-HH.0.

C.d.F. and L.F. have been partially funded by the Italian Research Center on High-Performance Computing, Big Data and Quantum Computing (ICSC), European Union - Next Generation EU.

The present research is within the framework of the project "Dipartimento di Eccellenza 2023-2027" granted by Italian MUR.

Finally, we thank Davide Galimberti for the implementation of a preliminary version of the scheme.

Conflict of interest

The authors declare that they have no potential conflict of interest.

A Asymptotic stability analysis of the IMEX-ARK Galerkin scheme

Let us consider the one-dimensional linear advection problem with reaction term

$$\partial_t q + a\partial_x q + \gamma q = 0, \tag{25}$$

where q is a generic scalar conservation variable, and a, γ are real coefficients. The coefficient γ is assumed to be strictly positive as it physically represents a friction in the model equation. In the following, we consider a uniform mesh with size Δx, with i we indicate a generic mesh node, which is shared by two consecutive cells indicated with $i-\frac{1}{2}$ and $i+\frac{1}{2}$.

We first analyze the stability of the IMEX-ARK Galerkin method described in [4] (section 3.1) which employs the Additive RK.2.A.2 described in [19] in combination with the Galerkin method on the discrete spaces $\mathbb{Q}_0$, $\tilde{\mathbb{Q}}_1$. For each spatial node and for each time t^n we have

$$\begin{cases} q_{i+\frac{1}{2}}^{n+\frac{1}{2}} = \dfrac{q_i^n + q_{i+1}^n}{2} - \dfrac{\nu}{2}(q_{i+1}^n - q_i^n) - \dfrac{\Phi}{2} q_{i+\frac{1}{2}}^{n+\frac{1}{2}}, \\ q_i^{n+1} = q_i^n + \nu(q_{i-\frac{1}{2}}^{n+\frac{1}{2}} - q_{i+\frac{1}{2}}^{n+\frac{1}{2}}) - \dfrac{\Phi}{2}(q_i^n + q_{i+1}^n). \end{cases} \tag{26}$$

By combining the two equations above, we obtain the amplification factor, and by introducing the adimensional coefficients $\nu = a\frac{\Delta t}{\Delta x}$ and $\Phi = \gamma \Delta t$, after applying the von Neumann analysis to (26), we obtain the amplification factor

$$G = \frac{1}{1+\frac{\Phi}{2}} \left[1 - \frac{\Phi}{2} - \frac{2j\nu \sin\theta}{1+\frac{\Phi}{2}} + \frac{\nu^2}{1+\frac{\Phi}{2}}(\cos\theta - 1) \right], \tag{27}$$

with j the imaginary unit and θ an angle in $[0, \pi]$. In case of severe stiffness, i.e., by computing the amplification factor in the limit case $\Phi \to \infty$, the leading order term of the amplification factor results in

$$G \sim \frac{1-\frac{\Phi}{2}}{1+\frac{\Phi}{2}} = -1, \quad \text{as } \Phi \to \infty, \tag{28}$$

this under the hypothesis that ν is limited, i.e., $\nu = o(\sqrt{\Phi})$. Here, we set $\nu \in (0, 1]$. We note that the amplification factor does not decay as $\Phi \to \infty$. Indeed, when applying this kind of discretization to the real case study we have

presented in section 4.2, we experience oscillations in the mass flux and, eventually, a time step that continuously decrease reaching the epsilon machine.

Let us now focus on the IMEX-ARK discretization we have used in this work, i.e., the Additive RK.2.L.1 described in [19] in combinaion with the discretization spaces $\mathbb{Q}_0$, $\tilde{\mathbb{Q}}_1$. Again, for each time t^n we have the following set of discrete equations,

$$\begin{cases} q_{i+\frac{1}{2}}^{n+\frac{1}{2}} = \dfrac{q_i^n + q_{i+1}^n}{2} - \dfrac{\nu}{2}(q_{i+1}^n - q_i^n) - \dfrac{\Phi}{2}\left(\sqrt{2}-1\right)\dfrac{q_i^n + q_{i+1}^n}{2} - \Phi\left(1-\frac{\sqrt{2}}{2}\right) q_{i+\frac{1}{2}}^{n+\frac{1}{2}}, \\ \\ q_i^{n+1} = q_i^n + \nu(q_{i-\frac{1}{2}}^{n+\frac{1}{2}} - q_{i+\frac{1}{2}}^{n+\frac{1}{2}}) - \Phi\left(1-\frac{\sqrt{2}}{2}\right)(q_i^n + q_i^{n+1}) - \Phi(\sqrt{2}-1)\dfrac{q_{i+\frac{1}{2}}^{n+\frac{1}{2}} + q_{i-\frac{1}{2}}^{n+\frac{1}{2}}}{2}. \end{cases} \tag{29}$$

By applying the the Von Neumann analysis, we have the following amplification factor

$$G = \frac{1}{1+\Phi\left(1-\frac{\sqrt{2}}{2}\right)}\Bigg[1-\Phi\left(1-\frac{\sqrt{2}}{2}\right) + \frac{\nu}{1+\Phi\left(1-\frac{\sqrt{2}}{2}\right)}\left(-j\sin\theta + \nu(\cos\theta-1) + \frac{\Phi}{2}(\sqrt{2}-1)j\sin\theta\right) + \\ - \frac{\frac{1}{2}\Phi(\sqrt{2}-1)}{1+\Phi\left(1-\frac{\sqrt{2}}{2}\right)}\left(1+\cos\theta - \nu j\sin\theta - \frac{\Phi}{2}(\sqrt{2}-1)(\cos\theta+1)\right)\Bigg], \tag{30}$$

which reduces to

$$G \sim -1 + \frac{1}{4}\left(\frac{\sqrt{2}-1}{1-\frac{\sqrt{2}}{2}}\right)^2(1+\cos\theta), \quad \text{as } \Phi\to\infty. \tag{31}$$

The asymptotic limit of the amplification factor coincides with equation (28) in the case $\theta = \pi$. In any case we note that this situation is rather unlikely to happen because it corresponds to the case $2q_i^n + q_{i-1}^n + q_{i+1}^n = 0$ so it means that locally we are in presence of a change of sign of the conserved variable. In all the other situations the asymptotic limit in (31) is always lower than one in modulus, and approaches zero for values of θ close to zero.

References

[1] A. Costa, G. Macedonio, Computational modeling of lava flows: A review, Special papers-Geological Society of America 396 (2005) 209.

[2] E. Biagioli, M. d. Vitturi, F. Di Benedetto, Modified shallow water model for viscous fluids and positivity preserving numerical approximation, Applied Mathematical Modelling 94 (2021) 482–505.

[3] C. J. Conroy, E. Lev, A discontinuous galerkin finite-element model for fast channelized lava flows v1. 0, Geoscientific Model Development 14 (6) (2021) 3553–3575.

[4] F. Gatti, C. de Falco, S. Perotto, L. Formaggia, M. Pastor, A scalable well-balanced numerical scheme for the modeling of two-phase shallow granular landslide consolidation, Journal of Computational Physics 501 (2024) 112798.

[5] M. Quecedo, M. Pastor, A reappraisal of Taylor–Galerkin algorithm for drying–wetting areas in shallow water computations, International Journal for Numerical Methods in Fluids 38 (6) (2002) 515–531.

[6] F. Gatti, M. Fois, C. de Falco, S. Perotto, L. Formaggia, Parallel simulations for fast-moving landslides: space-time mesh adaptation and sharp tracking of the wetting front, International Journal for Numerical Methods in Fluids (2023).

[7] F. Gatti, L. Bonaventura, A. Menafoglio, M. Papini, L. Longoni, A fully coupled superficial runoff and soil erosion basin scale model with efficient time stepping, Computers & Geosciences 177 (2023) 105362.

[8] S. Soares-Frazão, J. Lhomme, V. Guinot, Y. Zech, Two-dimensional shallow-water model with porosity for urban flood modelling, Journal of Hydraulic Research 46 (1) (2008) 45–64.

[9] C. Parés, Numerical methods for nonconservative hyperbolic systems: a theoretical framework., SIAM Journal on Numerical Analysis 44 (1) (2006) 300–321.

[10] M. J. Castro, E. D. Fernández-Nieto, A. M. Ferreiro, J. A. García-Rodríguez, C. Parés, High order extensions of Roe schemes for two-dimensional nonconservative hyperbolic systems, Journal of Scientific Computing 39 (2009) 67–114.

[11] M. Castro, J. M. Gallardo, J. A. López-GarcÍa, C. Parés, Well-balanced high order extensions of Godunov's method for semilinear balance laws, SIAM Journal on Numerical Analysis 46 (2) (2008) 1012–1039.

[12] J. M. Gallardo, C. Parés, M. Castro, On a well-balanced high-order finite volume scheme for shallow water equations with topography and dry areas, Journal of Computational Physics 227 (1) (2007) 574–601.

[13] M. Dumbser, E. F. Toro, A simple extension of the Osher Riemann solver to non-conservative hyperbolic systems, Journal of Scientific Computing 48 (1) (2011) 70–88.

[14] S. Busto, M. Dumbser, S. Gavrilyuk, K. Ivanova, On thermodynamically compatible finite volume methods and path-conservative ADER discontinuous Galerkin schemes for turbulent shallow water flows, Journal of Scientific Computing 88 (1) (2021) 28.

[15] F. Gatti, C. de Falco, S. Perotto, L. Formaggia, A scalable well-balanced numerical scheme for the simulation of fast landslides with efficient time stepping, Applied Mathematics and Computation 468 (2024) 128525.

[16] A. Costa, Numerical simulation of lava flows based on depth-averaged equations, Geophysical Research Letters 32 (5) (2005). doi:10.1029/2004gl021817.

[17] J.-F. Gerbeau, B. Perthame, Derivation of viscous Saint-Venant system for laminar shallow water; numerical validation, Ph.D. thesis, INRIA (2000).

[18] S. Ferrari, F. Saleri, A new two-dimensional shallow water model including pressure effects and slow varying bottom topography, ESAIM: Mathematical Modelling and Numerical Analysis 38 (2) (2004) 211–234.

[19] H. Liu, J. Zou, Some new additive Runge-Kutta methods and their applications, Journal of Computational and Applied Mathematics 190 (1) (2006) 74–98, special Issue: International Conference on Mathematics and its Application.

[20] F. Fambri, A novel structure preserving semi-implicit finite volume method for viscous and resistive magnetohydrodynamics, International Journal for Numerical Methods in Fluids 93 (12) (2021) 3447–3489.

[21] G. Tumolo, L. Bonaventura, A semi-implicit, semi-Lagrangian discontinuous Galerkin framework for adaptive numerical weather prediction, Quarterly Journal of the Royal Meteorological Society 141 (692) (2015) 2582–2601.

[22] G. Orlando, P. F. Barbante, L. Bonaventura, An efficient IMEX-DG solver for the compressible Navier-Stokes equations for non-ideal gases, Journal of Computational Physics 471 (2022) 111653.

[23] W. Boscheri, A. Chiozzi, M. G. Carlino, G. Bertaglia, A new family of semi-implicit Finite Volume/Virtual Element methods for incompressible flows on unstructured meshes, Computer Methods in Applied Mechanics and Engineering 414 (2023) 116140.

[24] S. T. Zalesak, Fully multidimensional flux-corrected transport algorithms for fluids, Journal of Computational Physics 31 (3) (1979) 335–362.

[25] J. P. Boris, D. L. Book, Flux-corrected transport. iii. Minimal-error FCT algorithms, Journal of Computational Physics 20 (4) (1976) 397–431.

[26] D. Kuzmin, M. Möller, S. Turek, High-resolution FEM–FCT schemes for multidimensional conservation laws, Computer Methods in Applied Mechanics and Engineering 193 (45-47) (2004) 4915–4946.

[27] M. Castro, A. Pardo, C. Parés, E. Toro, On some fast well-balanced first order solvers for nonconservative systems, Mathematics of computation 79 (271) (2010) 1427–1472.

[28] Y. Xing, C.-W. Shu, A new approach of high order well-balanced finite volume WENO schemes and discontinuous Galerkin methods for a class of hyperbolic systems with source terms, Comput. Phys 1 (1) (2006) 100–134.

[29] P. Saramito, C. Smutek, B. Cordonnier, Numerical modeling of shallow non-newtonian flows: Part i. the 1d horizontal dam break problem revisited, International Journal of Numerical Analysis & Modeling, Series B 4 (3) (2013) 283–298.

[30] G. Ganci, A. Cappello, V. Zago, G. Bilotta, A. Herault, C. Dal Negro, 3D Lava flow mapping of the 17-25 May 2016 Etna eruption using tri-stereo optical satellite data, Annals of Geophysics (2019).

[31] A. Rohatgi, Webplotdigitizer: Version 4.6 (2022).
URL `https://automeris.io/WebPlotDigitizer`

[32] B. Sudret, Global sensitivity analysis using polynomial chaos expansions, Reliability engineering & system safety 93 (7) (2008) 964–979.

MOX Technical Reports, last issues

Dipartimento di Matematica
Politecnico di Milano, Via Bonardi 9 - 20133 Milano (Italy)

21/2024 Caldana, M.; Antonietti P. F.; Dede' L.
Discovering Artificial Viscosity Models for Discontinuous Galerkin Approximation of Conservation Laws using Physics-Informed Machine Learning

19/2024 Torzoni, M.; Manzoni, A.; Mariani, S.
A multi-fidelity surrogate model for structural health monitoring exploiting model order reduction and artificial neural networks

20/2024 Torzoni, M.; Manzoni, A.; Mariani, S.
Structural health monitoring of civil structures: A diagnostic framework powered by deep metric learning

17/2024 Fois, M.; de Falco, C.; Formaggia, L.
A semi-conservative depth-averaged Material Point Method for fast flow-like landslides and mudflows

16/2024 Domanin D. A.; Pegoraro M.; Trimarchi S.; Domanin M.; Secchi P.
Persistence diagrams for exploring the shape variability of abdominal aortic aneurysms

15/2024 Vaccaro, F.; Mauri, A.G.; Perotto, S.; Brivio, S.; Spiga, S.
Modeling and simulation of electrochemical and surface diffusion effects in filamentary cation-based resistive memory devices

14/2024 Zappon, E.; Salvador, M.; Piersanti, R.; Regazzoni, F.; Dede', L.; Quarteroni, A.
An integrated heart-torso electromechanical model for the simulation of electrophysiological outputs accounting for myocardial deformation

12/2024 Zingaro, A.; Ahmad, Z.; Kholmovski, E.; Sakata, K.; Dede', L.; Morris, A.K.; Quarteroni, A.; Trayanova, N.A.
A comprehensive stroke risk assessment by combining atrial computational fluid dynamics simulations and functional patient data

Antonietti, P.F.; Corti, M.
Numerical modelling of protein misfolding in neurodegenerative diseases a computational study

11/2024 Antonietti, P.F.; Corti, M.
Numerical modelling of protein misfolding in neurodegenerative diseases: a computational study